

# **Effect of Deflagration-to-Detonation Transition on Pulse Detonation Engine Impulse**

M. Cooper, S. Jackson, J. E. Shepherd

May 30, 2000

GALCIT Report FM00-3

Explosion Dynamics Laboratory  
Graduate Aeronautical Laboratories  
California Institute of Technology  
Pasadena, CA 91125 USA

## Table of Contents

Abstract	5
1.0 Introduction	6
1.1 Deflagration-to-Detonation Transition	6
1.2 Effect of Tube Walls on DDT	7
1.3 Previous Research	8
1.4 Purpose of Current Research	8
2.0 Experimental Setup	9
2.1 Instrumentation of Detonation Tube	9
2.1.1 Ionization Probes	10
2.1.2 Pressure Transducers	11
2.1.3 Ignition System	11
2.1.4 Ballistic Pendulum Arrangement	12
2.1.5 Obstacle Configurations	12
2.1.5.1 Blockage Plate Configuration	12
2.1.5.2 Orifice Plate Configurations	13
3.0 Experimental Procedure	14
4.0 Theory and Analysis	15
4.1 DDT Time and Distance Determination	15
4.2 Ballistic Impulse Determination	15
4.3 Pressure Impulse Determination	16
4.4 Theoretical Model	18
4.4.1 Impulse Calculation	19
4.4.2 Determination of $\alpha$	20
4.4.3 Determination of b	21
4.4.4 Summary	21
5.0 Results	22
5.1 DDT Time and Distances	22
5.1.1 Time-Space and Velocity Space Trends	22
5.1.2 DDT Distance	22
5.1.3 DDT Time	23
5.2 Impulse	24
5.2.1 Effect of Diluent Concentration, Pressure and Obstacle Configurations on Impulse	24
5.2.1.1 Effect of Diluent Concentration	24
5.2.1.2 Effect of Mixture Pressure	25
5.2.1.3 Effect of Obstacles	25
5.2.2 Comparison of Ballistic and Pressure Impulse Methods	25
5.2.3 Theoretical Impulse Model	27
6.0 Discussion and Conclusions	28
6.1 DDT Distances and DDT Times	28
6.2 Impulse	28
6.2.1 Effect of Diluent Concentration, Pressure and Obstacle Configurations on Impulse	28
6.2.2 Comparison of Ballistic and Pressure Impulse Methods	28

6.2.3 Theoretical Impulse Model	28
6.2.4 Additional Loss Mechanisms	29
6.3 Future Work	29
7.0 Acknowledgement	31
Appendix A	
Appendix B	
Appendix C	
Appendix D	
Appendix E	

## List of Figures

Figure 1. Four Steps of a Pulse Detonation Engine Cycle
Figure 2. Steps from deflagration to detonation
Figure 3. Mechanical drawing of detonation tube
Figure 4. Block diagram of experimental setup
Figure 5. Ionization probe circuit
Figure 6. Mechanical drawing of front wall end cap (units in inches)
Figure 7. Ballistic pendulum arrangement for the initial and fully deflected positions
Figure 8. Components of blockage plate obstacles (units in inches)
Figure 9. Blockage plate obstacle configuration
Figure 10. Drawing of orifice plate with 0.43 blockage ratio (units in inches)
Figure 11. Orifice plate obstacle configuration (full) with 0.43 blockage ratio
Figure 12. Orifice plate obstacle configuration (half) with 0.43 blockage ratio
Figure 13. Time-distance diagram illustrating several combustion waves
Figure 14. Important parameters in impulse determination
Figure 15. Control volume for rocket
Figure 16. Pulse detonation engine control volume
Figure 17. Sample pressure trace from the first transducer
Figure 18. X-T diagram inside detonation tube
Figure 19. Idealized pressure trace
Figure 20. Refined pressure trace
Figure 21. Time versus space plot for varying diluent and no obstacles
Figure 22. Velocity versus space plot for varying initial pressure and no obstacles
Figure 23. DDT distance versus % diluent and obstacle configurations
Figure 24. DDT distance versus pressure and obstacle configurations
Figure 25. DDT time for varying diluent and obstacle configurations
Figure 26. DDT time versus pressure and obstacle configurations
Figure 27. Impulse for varying diluent and obstacle configurations
Figure 28. Impulse versus pressure and obstacle configurations

Figure 29. Comparison of drag due to internal obstacles  
Figure 30. Late DDT

## **List of Tables**

Table 1. List of equipment used

## Abstract

A detonation tube was built to study the deflagration-to-detonation transition (DDT) process and the impulse generated when combustion products exhaust into the atmosphere. The reactants used were stoichiometric ethylene and oxygen mixture with varying amounts of nitrogen present as diluent. The effects of varying the initial pressure from 30 kPa to 100 kPa were studied, as were the effects of varying the diluent concentration from 0% to 73.8% of the total mixture. Measurements were carried out with the tube free of obstacles and with three different obstacle configurations. Each obstacle configuration had a blockage ratio of 0.43.

It was found that the inclusion of obstacles dramatically lowered the DDT times and distances as compared to the no obstacle configuration. The obstacles were found to be particularly effective at inducing DDT in mixtures with low pressures and with high amounts of diluent. At the lowest pressures tested (30 kPa), obstacles reduced the DDT time and distance to approximately 12.5% of the no obstacle configuration values. The obstacles also allowed DDT to occur in mixture compositions of up to 60% diluent, while DDT was not achieved with more than 30% diluent in the no obstacle configuration.

A ballistic pendulum arrangement was utilized, enabling direct measurement of the impulse by measuring the tube's deflection. Additional means of impulse comparison consisted of integrating the pressure over the front wall of the tube. Impulse measurements were then compared with a theoretical model and were found to fit well cases that did not contain internal obstacles.

The inclusion of obstacles allowed DDT to occur in mixtures with high amounts of diluent where DDT was not observed to occur in the cases without obstacles. Roughly 100% more impulse was produced in the obstacle configurations as compared to the no obstacle configuration under these conditions. In instances where DDT occurred in the no obstacle configuration, the use of obstacle configurations lowered the impulse produced by an average of 25%. For cases where no obstacles were used and DDT occurred, the pressure derived impulses (pressure impulse) and impulses determined from the ballistic pendulum (ballistic impulses) are similar. For cases where obstacle configurations were tested, pressure impulses were more than 100% higher on average than ballistic impulses. This difference exists because the pressure model neglects drag due to the obstacle configurations.

## 1.0 Introduction

Current detonation research is focused strongly around pulse detonation engine development. A pulse detonation engine is an unsteady propulsive device that contains four major steps per cycle. These steps appear in figure 1. The first step consists of filling a combustion chamber with combustible gases and initiating detonation. In the second step, the detonation wave propagates to the open end of the tube followed by the Taylor wave. The third step begins with the reflection of the expansion wave off the interface. This reflected expansion immediately interacts with the Taylor wave, while the products begin to exhaust the tube. The fourth step consists of the first characteristic of the reflected expansion reaching the front wall of the tube thus decreasing the pressure at this wall.

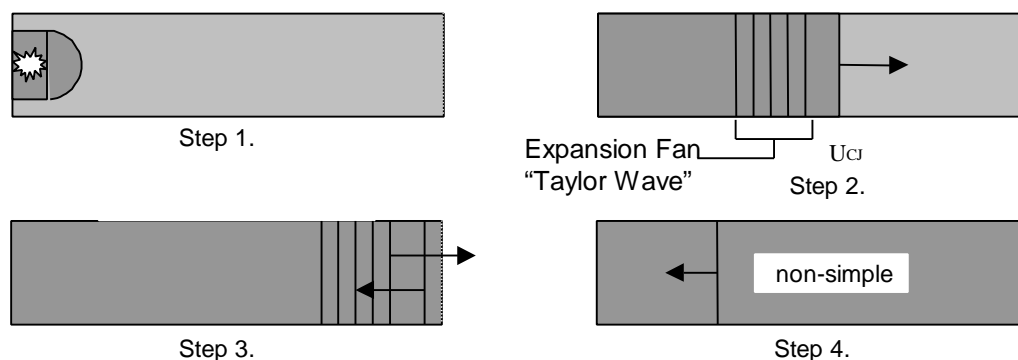


Figure 1. Four steps of a pulse detonation engine cycle

Thrust is generated as the combustion products exit the tube. By operating the engine at a high cycle frequency and/or having multiple combustion chambers it is feasible to establish a regime of quasi-steady thrust.

### 1.1 Deflagration-to-Detonation Transition

A detonation may be initiated by two different modes: deflagration-to-detonation transition and direct initiation. This research focuses on the deflagration-to-detonation transition (DDT) which is characterized by the DDT time and distance. A detonation, formed in a tube that is ignited at a closed end, begins with a combustion wave that accelerates due to heating of the unburned gases ahead of the wave. This heating occurs from successive compressive waves formed from the expansion of the burned gas products, which have a specific volume that is 10-15 times greater than the unburned gases ahead of the flame. The higher temperature of the unburned gases causes the sound velocity to increase enabling the succeeding waves to catch up to the initial wave. The higher temperature in the unburned gases also contributes to increasing the flame speed, accelerating the unburned mixture. Turbulence in the flow initiates due to this unburned gas acceleration, the natural instability of high Reynolds number flows and the vortices associated with flow over defects or obstructions in the tube. This turbulence causes a distortion of the flame front. As flow turbulence in the tube increases, additional

increases in the velocity and acceleration cause the formation of additional compression waves in addition to further distorting the flame front separating it into distinct sheets.

The positive feedback between the flame and the flow ahead of it progresses to a point where the flame breaks into a distributed reaction zone with strong straining motions and large fluctuations in the temperature and species concentrations at the characteristic flame scale length. Some portions of the flame front are extinguished due to the locally high strain rates. As parts of the previously extinguished mixture re-ignite in the form of exploding eddies; weak shock waves are formed ahead of the front. At this point the burning rate increases slightly and the interaction of reaction waves, hotspots, and the amplification of weak shock waves results in the reactants exploding close behind the shock. This energy release is sufficient to maintain the shock's strength, thus forming a detonation.

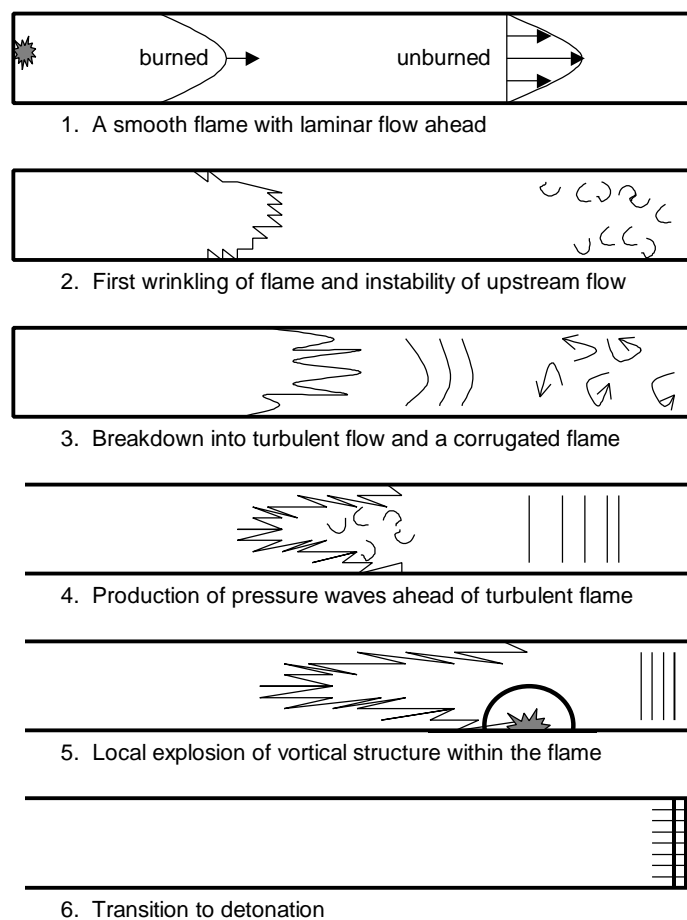


Figure 2. Steps from deflagration to detonation

## 1.2 Effect of Tube Walls on DDT

The onset of detonation differs in smooth and rough tubes. In smooth tubes, an abrupt change in the propagation speed occurs. A pre-detonation flame velocity is typically 1000 m/s while the characteristic Chapman-Jouguet (C-J) detonation speed is over 2000

m/s. This C-J detonation velocity arises by solving the integrated conservation equations by assuming the detonation wave is steady, planar and one-dimensional. Under these conditions, the flow behind a supersonic detonation is sonic. A large explosion occurs at the onset of detonation resulting in an over-driven detonation wave that decays to the C-J velocity. In rough tubes, the flame acceleration is more rapid and not as clearly marked by an abrupt velocity change. The wall roughness controls the wave propagation by inducing large-amplitude unsteady and turbulent flow, complex wave interaction processes and high temperatures behind shock reflections. These effects represent ways that the flow can generate large-scale turbulence for flame folding and large temperature fluctuations causing detonation initiation.

### **1.3 Previous Research**

Prior research has been completed utilizing the ballistic pendulum setup with different sized tubes. Tube geometries tested have included length to internal diameter ratios of 40 and 8. The DDT testing was conducted with propane and acetylene. Two spirals were used as the internal obstacle configurations with different blockage ratios. Different regimes of detonation, DDT, quasi-detonation and fast flames were observed.

A theoretical model has been constructed to predict impulse from a one-cycle detonation engine. This model allows for different mixtures but does not account for the inclusion of internal obstacles. Further discussion of the model appears below in the theory and analysis section.

### **1.4 Purpose of Current Research**

The present study addresses the effect of different internal obstacle configurations on DDT times, DDT distances and resulting impulse for a range of initial pressures and dilution concentration. The experimental impulse measurements are calculated by two methods. The first method determines the impulse from the deflection in a ballistic pendulum setup. The second method determines the impulse by integrating the pressure force on the front wall of the detonation tube. These experimental results for the different obstacles are then compared with a theoretical model that predicts the impulse of a one-cycle pulse detonation engine for different mixtures.

By comparing the impulse measurements for the different internal obstacle configurations, several conclusions will be made regarding the ability of internal obstacles to affect DDT times, DDT distances and resulting impulse.

## 2.0 Experimental Setup

The experimental setup consists of a detonation tube instrumented with ionization probes and pressure transducers in a ballistic pendulum arrangement. The tube was constructed from 6061-T6 aluminum. It had an internal diameter of 0.0762 m, a wall thickness of 0.0127 m and a length of 1.016 m.

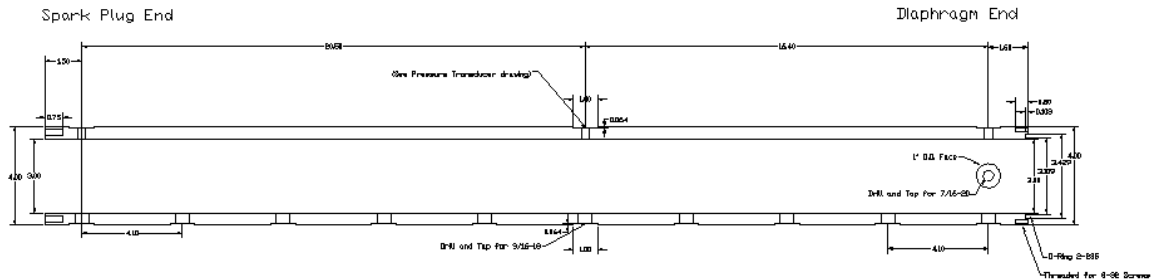


Figure 3. Mechanical drawing of detonation tube

## 2.1 Instrumentation of Detonation Tube

The detonation tube contains a total of 10 ionization probes and three pressure transducers. The signals from all the ionization probes were combined onto one scope channel while the signal from each pressure transducer was assigned to the remaining three scope channels. An oscilloscope sampling at a rate of 1 MHz was used to record the four signals. A block diagram of the experimental setup, including electrical wiring and plumbing, appears in Figure 4. A list of equipment used appears below in Table 1.

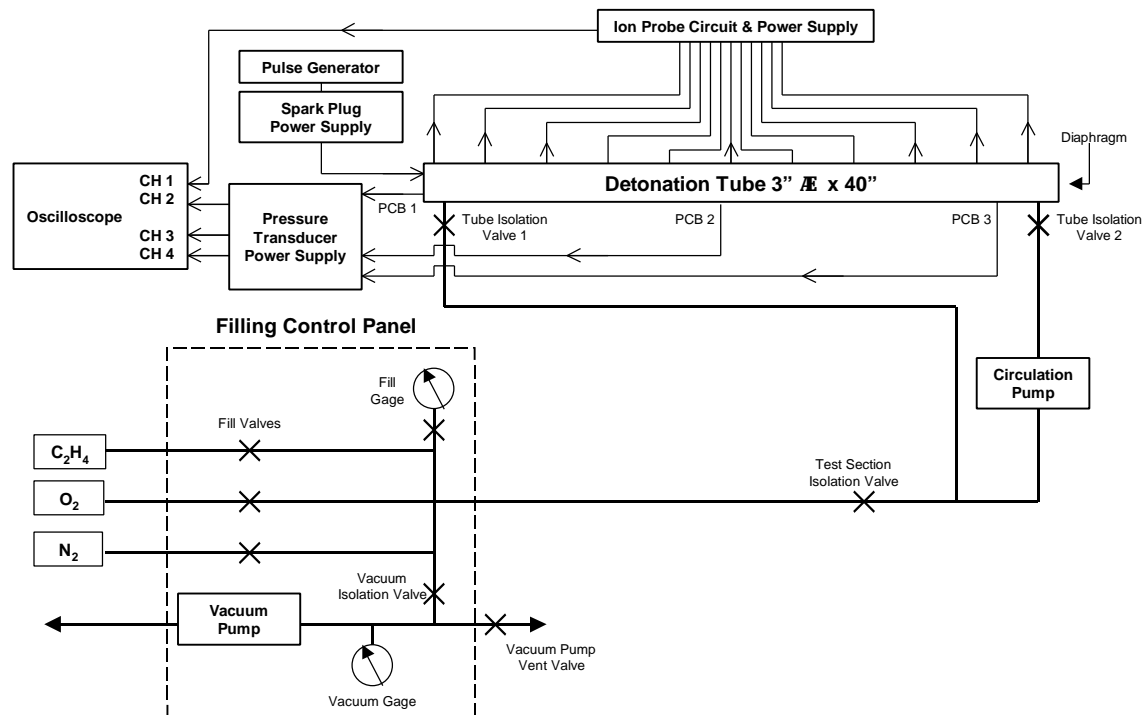


Figure 4. Block diagram of experimental setup

Table 1. List of equipment used

Filling Control Station	GALCIT – Explosion Dynamics Laboratory
Color Video Monitor (2)	Sony Trinitron PVM - 14N14
Video Cassette Recorder (2)	Panasonic AG – 1970
Camera (2)	Sony CCD - IRIS DXC – 107A
Camera Adapter (2)	Sony CMA - D2
Oscilloscope	Tektronix TDS 460A
Spark Plug Voltage Supply	GALCIT - Explosion Dynamics Laboratory
Pulse Generator	Stanford Research Systems, Inc. DG535
Pressure Transducers (3)	Piezotronics 113A26
Ionization Probes (10)	GALCIT - Explosion Dynamics Laboratory
Ionization Circuit Box	GALCIT - Explosion Dynamics Laboratory
Pressure Transducer Power Supply	Piezotronics 482A04
Power Supply for Ion Circuit Box	GALCIT - Explosion Dynamics Laboratory
Mixing Pump	MagneTek JB1P072N
Vacuum Pump	Duo Seal 1397
Piston Engine Spark Plug	Champion REJ38

### 2.1.1 Ionization Probes

A total of 10 ionization probes were located every 0.10414 m along the tube's length. The signals from the ten ionization probes were combined onto one scope channel. As the reaction zone travels past an ionization probe, the probe's pins are briefly shorted. By measuring the time between signal spikes of adjacent ion probes, the velocity of the combustion wave was determined. This value was compared with the C-J detonation velocities calculated from the STANJAN thermo-chemical equilibrium program (Reynolds 1986) to determine when transition to detonation occurred. The error associated with this experimental velocity measurement is less than  $\pm 0.0001\%$ .

An electrical circuit was designed so that the flame front shorting the probe's pins allowed a capacitor to discharge for the duration that the pins were shorted. The oscilloscope recorded this discharge. Figure 5 contains the circuit to do this.

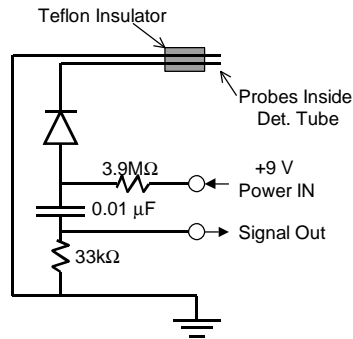


Figure 5. Ionization probe circuit

### 2.1.2 Pressure Transducers

The detonation tube was instrumented with three Piezotronics pressure transducers. The first transducer was installed in the front wall next to the ignition source. The signal from this transducer was utilized in the pressure integration method to determine the impulse. The second and third transducers were placed opposite the 6<sup>th</sup> and 10<sup>th</sup> ion probes respectively.

The pressure transducer calibrations from the manufacturer were applied to convert the raw voltage values to pressure values. This value had an error of  $\pm 0.5$  mV/psi.

### 2.1.3 Ignition System

A piston engine spark plug served as the tube's ignition source. This spark plug was mounted in the front wall end cap next to one of the gas fill lines and the first pressure transducer. Figure 6 shows this arrangement.

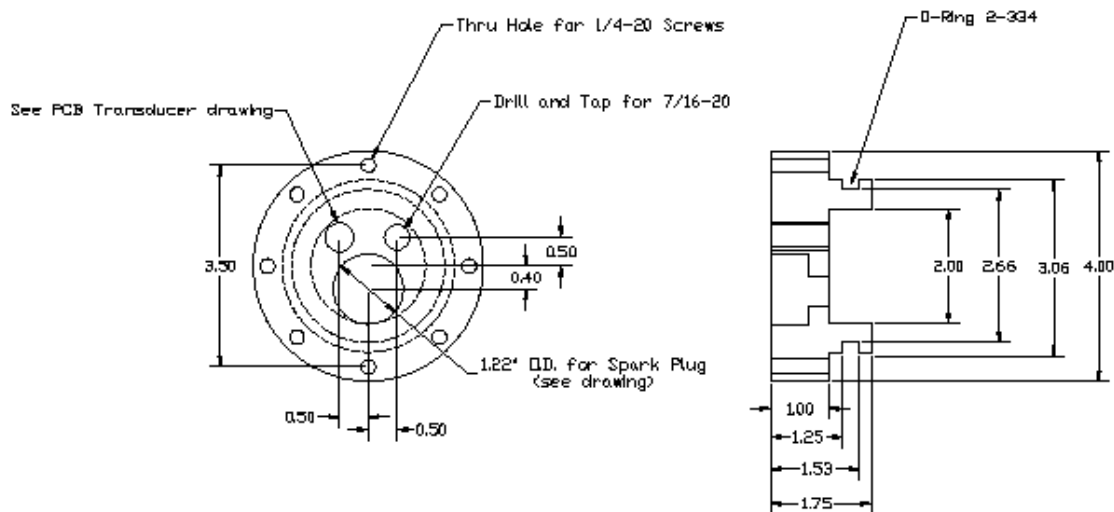


Figure 6. Mechanical drawing of front wall end cap (units in inches)

A 5  $\mu\text{F}$  capacitor charged at 110V (total stored energy of 30 mJ) discharged through a 163:1 trigger transformer. This provided the required energy to ignite the spark plug.

#### 2.1.4 Ballistic Pendulum Arrangement

The tube was suspended from steel wires to create a ballistic pendulum arrangement as shown in Figure 7.

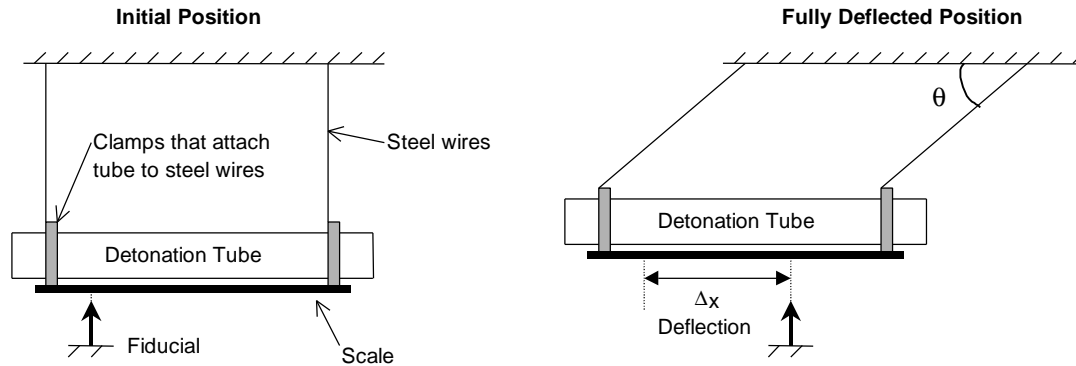


Figure 7. Ballistic pendulum arrangement for the initial and fully deflected positions

This setup enabled an additional measure of the impulse by recording the deflection,  $\Delta x$ , with a camera. The camera recorded the position measurement at the location of a fiducial mounted on a table under the swinging detonation tube. A scale, attached to the tube clamps, enabled a precise measurement of the tube's deflection. This deflection measurement was assigned an error of  $\pm 0.5$  mm.

#### 2.1.5 Obstacle Configurations

Three obstacle configurations were built for testing in the detonation tube. Each obstacle had a blockage ratio of 0.43 and was designed to fit snugly within the tube's interior.

##### 2.1.5.1 Blockage Plate Configuration

The first obstacle configuration consisted of blockage plates spaced one tube diameter apart for the entire length of the detonation tube. Each blockage plate was suspended along the centerline of the tube with a single rod threaded through its center. The outer diameter of each plate was sized to generate the desired blockage ratio when installed in the detonation tube. The threaded rod connecting the plates was held into position by a support on each end of the rod and one support in the center of the rod. When the obstacle was installed in the tube, the end supports were flush against the inside lip of the front end cap and the lip of the diaphragm end plate thus preventing motion of the obstacles with respect to the tube. Figure 8 shows the dimensions of the blockage plate and the supports.



Blockage Plate with 0.43 Blockage Ratio      Support for Blockage Plate Obstacles  
 Figure 8. Components of blockage plate obstacles (units in inches)

The entire obstacle configuration appears in Figure 9 when the 11 blockage plates and three supports are threaded onto the rod.

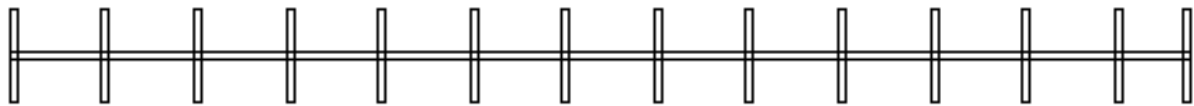


Figure 9. Blockage plate obstacle configuration

2.1.5.2 Orifice Plate Configurations

The second and third obstacle configurations utilized orifice plates. These orifice plates have an outer diameter matching the tube’s inner diameter. A hole through the center of the orifice plates was sized to generate the desired blockage ratio equal to that of the blockage plates. Figure 10 shows a drawing of the orifice plates.

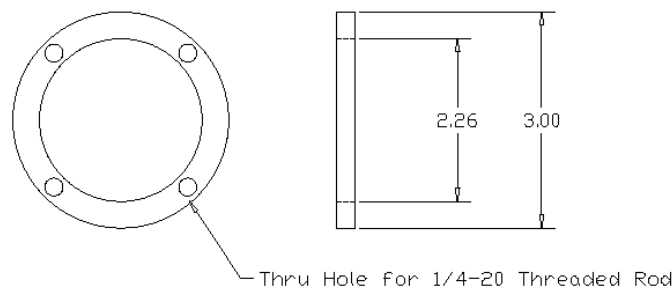


Figure 10. Drawing of orifice plate with 0.43 blockage ratio (units in inches)

The four through holes in each plate allows for them to be spaced one tube diameter apart with four threaded rods. Two different obstacle configurations were created using the same orifice plates. The first configuration, shown in Figure 11, consists of 14 orifice plates spaced over the entire length of the tube. The first and last plates rest snugly against the front wall lip of the spark plug end cap and the lip of the diaphragm end cap.

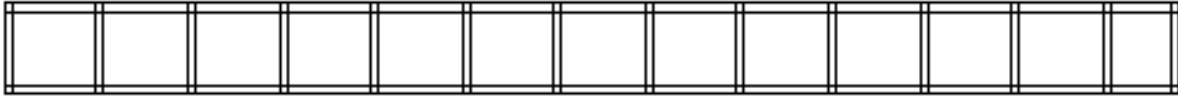


Figure 11. Orifice plate obstacle configuration (full) with 0.43 blockage ratio

A second configuration, shown in Figure 12, consists of only 8 orifice plates. Two of the plates are at the ends of the threaded rod to support the obstacle against the front wall lip of the spark plug end cap and the lip of the diaphragm end cap. The remaining 6 orifice plates were spaced one tube diameter apart, beginning at the spark plug tube end and ending near the middle point of the tube.

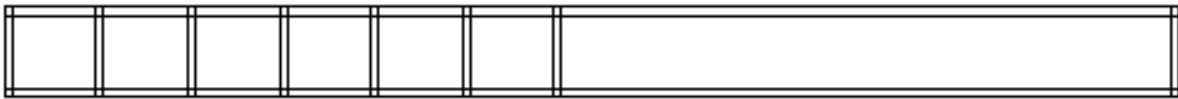


Figure 12. Orifice plate obstacle configuration (half) with 0.43 blockage ratio

### 3.0 Experimental Procedure

Each test began by installing a Mylar diaphragm (1 mil thickness) onto the tube with the diaphragm end plate. This diaphragm enabled the tube to be evacuated to an initial pressure less than 150 mtorr. The gas mixtures investigated involved ethylene as the fuel, oxygen as the oxidizer and nitrogen as the diluent. The gases were filled with the partial pressure technique and a mixing pump was operated for 5 minutes to ensure the gases were thoroughly mixed. The test variables consisted of varying the initial pressure, percent dilution and obstacle configuration. During each test one camera recorded the tube's deflection as described above in the ballistic pendulum arrangement explanation. An additional camera recorded the end of the tube to allow imaging of the exhaust plume. A sample checklist and list of test runs appears in Appendix A.

## 4.0 Theory and Analysis

The procedures used in the evaluation of the experimental data are discussed in this section. Relevant theory behind the determination of the DDT distances and DDT times are presented. In addition, the impulse calculation methods used to determine the impulse from the ballistic pendulum and the pressure transducers are derived.

### 4.1 DDT Time and Distance Determination

Characteristic shapes of different types of combustion waves on a space-time diagram are shown in Figure 13.

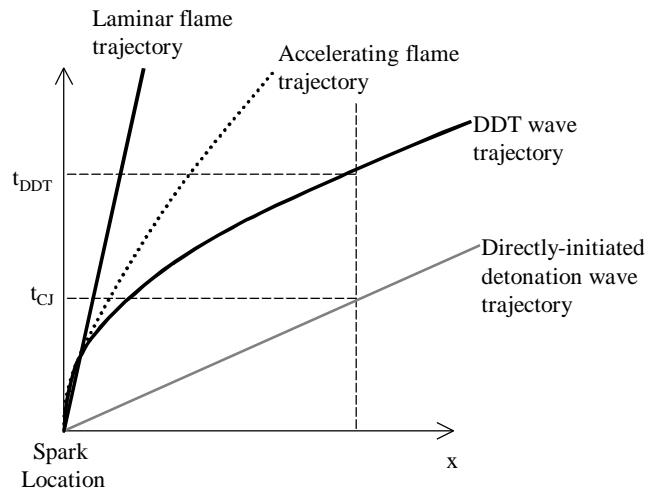


Figure 13. Time-distance diagram illustrating several combustion waves

The combustion wave velocity was determined by dividing the distance between ionization probes by the time it took the reaction zone to pass from one ionization probe to the next. This yielded an average velocity between the two probes. The combustion wave was defined as having undergone DDT when this average velocity was equal or greater than the C-J detonation velocity. The DDT distance was determined to be the midpoint between the two ionization probes. The times the flame arrived at each of these probes were averaged to obtain the DDT time. If the average velocity never attained  $U_{CJ}$ , then no DDT distance or DDT time was recorded. In this case, the combustion wave remained a deflagration.

### 4.2 Ballistic Impulse Determination

The first method to determine the impulse consisted of a ballistic pendulum arrangement where the tube was suspended by steel wires. The tube displacement was recorded with a camera focused on the fiducial. The impulse was then calculated using the pendulum equation, which is found via energy conservation in the following discussion.

Equating kinetic and potential energies, we see that

$$\frac{1}{2}mv^2 = mgh \quad [1]$$

where  $m$  is the mass of the pendulum bob,  $v$  is its velocity,  $g$  is gravitational acceleration and  $h$  is the height of the bob relative to the lowest point of its swing. Solving for velocity yields:

$$v = \sqrt{2gh} \quad [2]$$

Thus impulse can be found

$$I = mv = m\sqrt{2gh} \quad [3]$$

From Figure 17, it can be shown that

$$h = L(1 - \cos \mathbf{q}) = L \left( 1 - \sqrt{1 - \left( \frac{\Delta x}{L} \right)^2} \right) \quad [4]$$

Thus the pendulum equation is

$$I_{Pendulum} = Mass \sqrt{2gL \left( 1 - \sqrt{1 - \left( \frac{\Delta x}{L} \right)^2} \right)} \quad [5]$$

where  $\Delta x$  is the measured tube deflection and  $L$  is the length of the pendulum arm.

### 4.3 Pressure Impulse Determination

In determining the pressure impulse, several significant variables must be considered: the pressure profile, the mass flow rate and exit velocity, and shear stresses on the walls and obstacles.

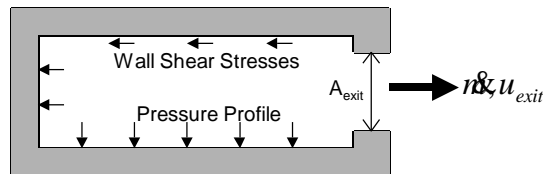


Figure 14. Important parameters in impulse determination

It is important to choose the appropriate control volume for our data. Following conventional rocket analysis, the control volume shown in Figure 15 can be analyzed.

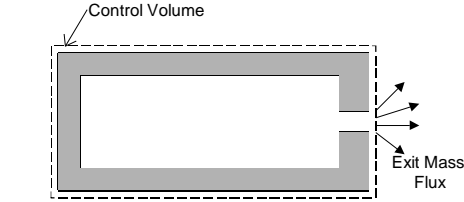


Figure 15. Control volume for rocket

Calculating the force balance, we see that at any given time:

$$F = \dot{m}_{exit} u_{exit} + A_{exit} (P_{exit} - P_{atm}) \quad [6]$$

To obtain impulse, equation 2 can be integrated with respect to time, yielding:

$$I = \int (\dot{m}_{exit} u_{exit} + A_{exit} (P_{exit} - P_{atm})) dt \quad [7]$$

However, the instrumentation of this experiment does not allow for direct measurement of  $\rho_{exit}$  or  $u_{exit}$ . Using the control volume shown in Figure 15, the force balance becomes:

$$F = (P_2 - P_1)A_1 + \sum \left( \int P dA \right)_{obstacles} + \int \tau dS + (P_2 - P_3)A_3 \quad [8]$$

where  $P_{obstacles}$  is the pressure profile over each obstacle,  $S$  is the wetted surface area of the inside of the tube and  $\tau$  is the shear stress at the tube surface.

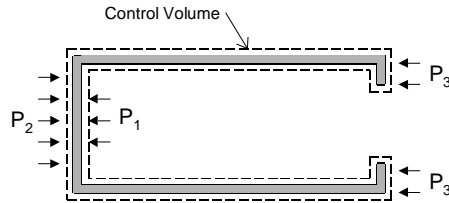


Figure 16. Pulse detonation engine control volume

These terms can be classified into three separate groups:

The force on the front wall of the tube is:

$$F_{front\_wall} = (P_2 - P_1)A_1 \quad [9]$$

The drag force is:

$$F_{drag} = \int \tau dS + \sum \left( \int P dA \right)_{obstacles} \quad [10]$$

And the force on the tube wall thickness (lip force):

$$F_{lip} = (P_2 - P_3)A_3 \quad [11]$$

Integration of the force balance yields the impulse:

$$I = \int F dt = I_{front\_wall} - I_{drag} - I_{lip} \quad [12]$$

This impulse equation is dependent on the pressure profile and the shear stress. The pressure profile can be determined from the pressure transducer measurements. The shear stress can be determined from comparison of pressure impulse with the ballistic impulse.

$$I_{ballistic} = I_{front\_wall} - I_{drag} \quad [13]$$

The above pressure integration is performed by numerically summing the area under the pressure curve for all time increments. A sample pressure trace from the first pressure transducer appears in Figure 17.

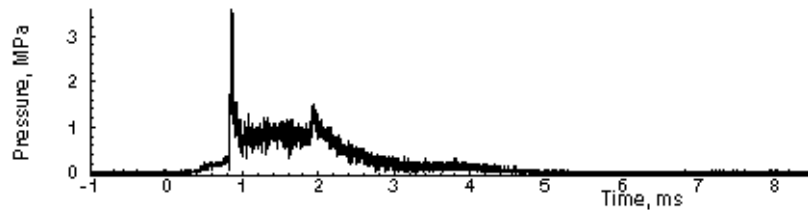


Figure 17. Sample pressure trace from the first transducer

#### 4.4 Theoretical Model

A theoretical model was created to predict the impulse value for a one-cycle pulse detonation engine for different mixtures. The following is summarized from Wintenberger (1999).

The x-t diagram in Figure 18 displays the detonation wave followed by the Taylor wave, as well as the first reflected characteristic off the mixture-air interface. This characteristic has an initial slope determined by the conditions at the interface, which is then modified by the interaction of the Taylor wave. Once it has passed through the Taylor wave, it propagates at the sound speed of the medium,  $c_3$ . Two times can be defined,  $t_1$  corresponding to the reflection of the shock wave at the interface, and  $t_2$  corresponding to the time necessary for the first reflected characteristic to go back to the thrust wall.

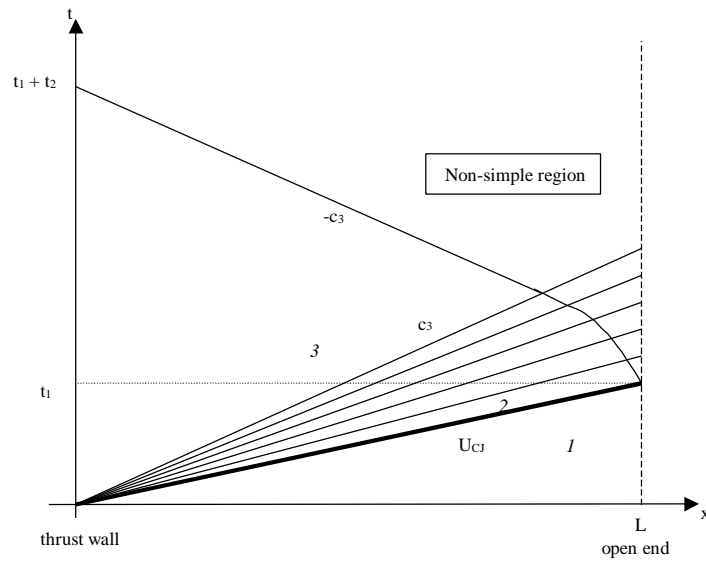


Figure 18. X-T diagram inside detonation tube

Figure 19 depicts the pressure trace expected from the idealized case. The C-J pressure peak is assumed instantaneous and the pressure immediately after drops to  $P_3$ . It remains  $P_3$  until the first reflected characteristic off the interface arrives back to the thrust wall, at a time  $t_1 + t_2$ . Then the pressure decreases since it is affected by the reflected expansion.

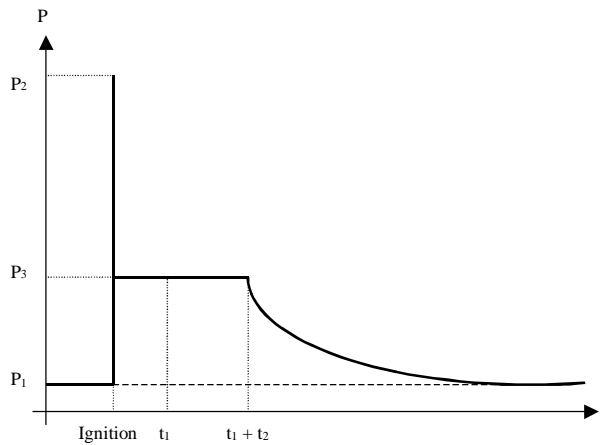


Figure 19. Idealized pressure trace

#### 4.4.1 Impulse Calculation

The impulse of a single-cycle pulse detonation engine is

$$I = A \int_0^{\infty} \Delta P(t) dt \quad [14]$$

where  $A$  is the area of the cross-section of the tube,  $DP$  is the pressure differential over the thrust wall. Ignition is assumed to occur at  $t = 0$ .

Considering the ideal pressure-time trace, the impulse can be decomposed as follows:

$$I = A \left[ \Delta P_3 (t_1 + t_2) + \int_{t_2}^{\infty} \Delta P(t) dt \right] \quad [15]$$

where  $t_1$  is the time for the detonation to reach the end of the tube ( $t_1 = L/U_{CJ}$ ),  $t_2$  is the time necessary for the first characteristic of the reflected wave to come back to the thrust wall. It depends on the length of the tube and the characteristic velocity behind the Taylor wave. The definition of  $t_2$  requires the introduction of a non-dimensional parameter,  $\alpha$ . Thus,  $t_2$  is defined as  $\alpha L/c_3$ .

The last part of the pressure-time integral will be non-dimensionalized with respect to  $c_3$ , as it is the characteristic velocity of the medium where the reflected wave propagates, and  $\Delta P_3$  so as to obtain a compact form for the impulse:

$$\int_{t_2}^{\infty} \Delta P(t) dt = \Delta P_3 t_3 = \Delta P_3 \beta L / c_3 \quad [16]$$

Where  $\beta$  is a second non-dimensional parameter used to describe this region.

Modeling of the decaying part of the pressure integral (gray area) by introducing a new characteristic time (dashed area) as shown in Figure 20:

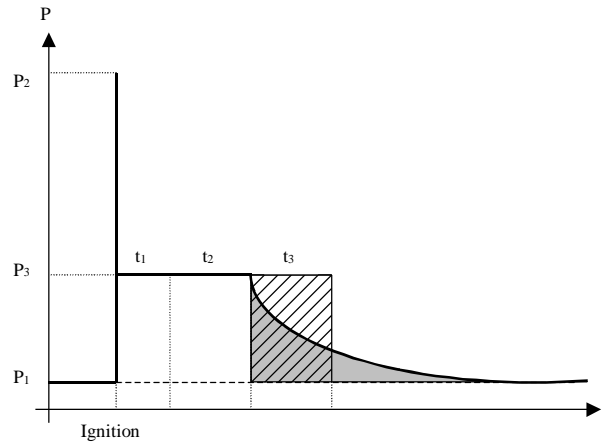


Figure 20. Refined pressure trace

So finally, the impulse can be written as:

$$I = A \Delta P_3 \left[ \frac{L}{U_{CJ}} + \alpha \frac{L}{c_3} + \beta \frac{L}{c_3} \right] \quad [17]$$

#### 4.4.2 Determination of $\alpha$

The non-dimensional parameter,  $\alpha$ , defines  $t_2 = \alpha L/c_3$ . The time,  $t_2$ , is the time necessary for the first characteristic of the reflected wave to arrive at the thrust wall. The interaction of this characteristic with the Taylor wave can be described by a similarity solution which generates the following analytical expression for  $\alpha$ :

$$\mathbf{a} = \frac{c_3}{U_{CJ}} \left[ 2 \left( \frac{\mathbf{g}-1}{\mathbf{g}+1} \left\{ \frac{c_3 - u_2}{c_2} + \frac{2}{\mathbf{g}-1} \right\} \right)^{\frac{\mathbf{g}+1}{2(\mathbf{g}-1)}} - 1 \right] \quad [18]$$

For stoichiometric C<sub>2</sub>H<sub>4</sub>-O<sub>2</sub> mixtures, the value of  $\alpha$  was found to be 1.13. Unsteady one-dimensional shock polars were used to calculate whether the reflected wave would be a shock or an expansion. In all mixtures considered, the reflected wave was an expansion.

All the quantities involved in this expression depend on the following two non-dimensional parameters:  $\mathbf{g}$  and the detonation Mach number  $M_{CJ} = U_{CJ}/c_1$ . The quantities behind the shock wave (labeled “2”) can be computed using the ideal gas model for a C-J detonation and the ones behind the Taylor wave are simply determined using the properties of the expansion fan. The resulting expression for  $\mathbf{a}$  in the ideal gas case is:

$$\mathbf{a}(\mathbf{g}M_{CJ}) = \frac{1}{2} \left( 1 + \frac{1}{M_{CJ}^2} \right) \left\{ 2 \left[ \frac{\mathbf{g}-1}{\mathbf{g}+1} \left( \frac{\mathbf{g}+3}{2} + \frac{2}{\mathbf{g}-1} - \frac{(\mathbf{g}+1)^2}{2} \frac{M_{CJ}^2}{1+\mathbf{g}M_{CJ}^2} \right) \right]^{\frac{\mathbf{g}+1}{2(\mathbf{g}-1)}} - 1 \right\} \quad [19]$$

#### 4.4.3 Determination of $\beta$

The reflected expansion fan interacts with the Taylor wave in a non-simple region, making it difficult to compute an analytical expression for  $\mathbf{b}$ . The only practical solution at the moment is therefore to rely on experimental data. Some data from Zitoun and Desbordes were used. They carried out experiments aimed at calculating the impulse of pulse detonation engines using tubes of different length. They showed that the impulse scales with the length of the tube. A pressure-time trace from their data was digitized and the relevant portion ( $t_2$  to  $t_3$ ) was integrated to obtain an estimate for  $\beta$ . For stoichiometric C<sub>2</sub>H<sub>4</sub>-O<sub>2</sub> mixtures, the value of  $\beta$  was found to be 0.53.

#### 4.4.4 Summary

Several conclusions were made from the analysis used to generate the theoretical model. The value of  $\mathbf{a}$  looks reliable. It was successfully checked against several sources of experimental data. The value of  $\mathbf{b}$  is less reliable. It is currently unknown whether the value is mixture dependent. A few numerical computations could be useful in the sense they would also determine a value for  $\mathbf{b}$ .

## 5.0 Results

The experimental results of DDT times, distances, and impulse are presented and analyzed in this section.

### 5.1 DDT Time and Distances

#### 5.1.1 Time-Space and Velocity-Space Trends

A time-space plot is shown in Figure 21. All additional time-space data is available in Appendix B. Decreasing slope indicates an accelerating flame. Linear trends indicate a constant velocity characteristic implying that detonation onset has occurred. The velocity-space plot, shown in Figure 22, demonstrates DDT velocity characteristics. All additional velocity-space data appears in Appendix C.

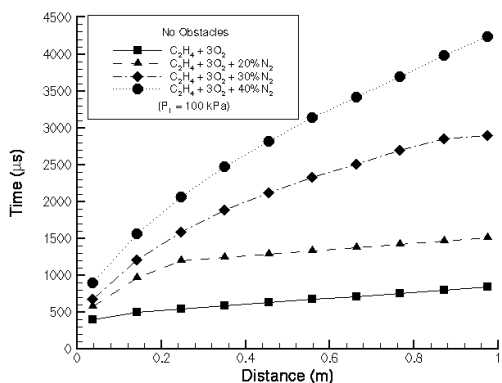


Figure 21. Time versus space plot for varying diluent and no obstacles

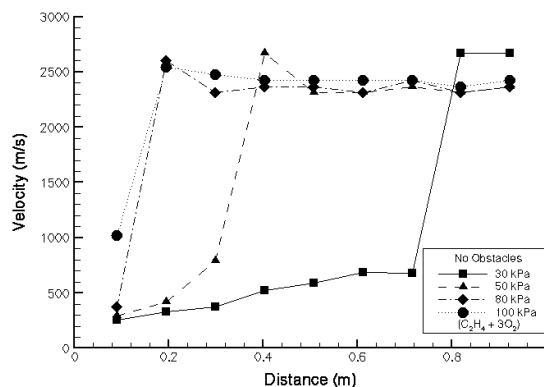


Figure 22. Velocity versus space plot for varying initial pressure and no obstacles

The combustion waves start out as deflagrations, moving at a relatively slow speed. As DDT occurs, the velocity rapidly jumps up to the detonation velocity. Sometimes the speed will exhibit a velocity spike, jumping above  $U_{CJ}$  just after DDT and remaining high for a short period of time before settling down to  $U_{CJ}$ . This is representative of an overdriven detonation wave which then reaches equilibrium. In cases where the velocity does not exhibit the rapid increase to  $U_{CJ}$ , DDT was not observed to occur.

#### 5.1.2 DDT Distance

DDT distance versus diluent concentration for stoichiometric ethylene-oxygen-nitrogen mixture is shown in Figure 23 for each obstacle configuration. All available DDT distance data appears in Appendix D. Experiments were performed over a range of 0% to 73.8% (air) diluent. DDT was not found to occur in mixtures made up of more than 30% diluent when the no obstacle configuration was used. When obstacles were used, the DDT range was increased to mixtures of 60% diluent.

DDT distance versus pressure for stoichiometric ethylene-oxygen mixture is shown in Figure 24 for each obstacle configuration. Experiments were performed over a range of 30 kPa to 100 kPa. The presence of obstacles seems to decrease the DDT distance. The effect of obstacles is not apparent for high pressures or low amounts of diluent. However, at a pressure of 30 kPa, the DDT distance with obstacles is reduced by as much as by one eighth as compared to the no obstacle DDT distance. At a diluent ratio of 30% the obstacle ration can be extrapolated to yield a DDT distance that is 30% of the no obstacle DDT distance. Furthermore, the use of obstacles allows DDT to occur over the diluent range of 30% to 60%; with no obstacles, DDT was not found to occur over this range. The experimental error makes it difficult to determine which obstacle configuration is more effective at causing the onset of DDT.

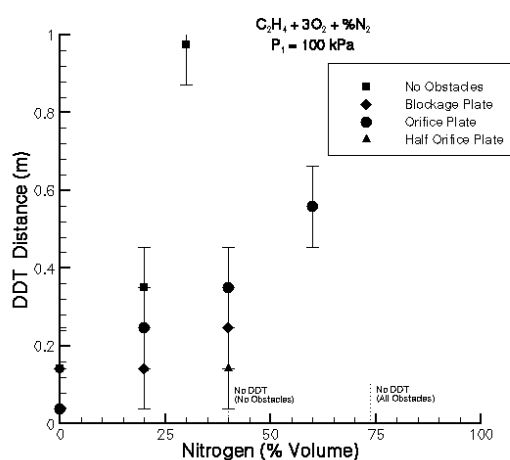


Figure 23. DDT distance versus % diluent and obstacle configurations

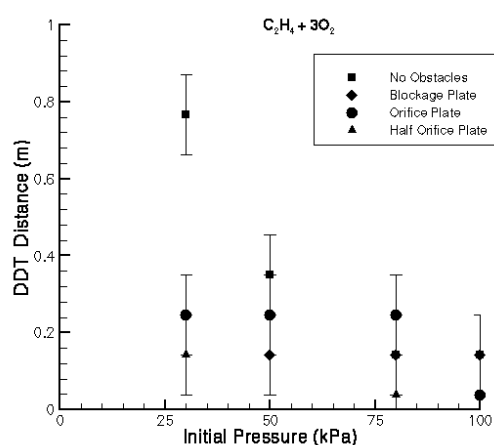
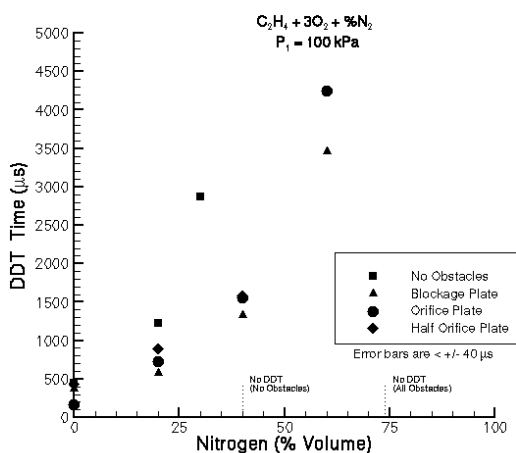


Figure 24. DDT distance versus pressure and obstacle configurations

### 5.1.3 DDT Time

DDT time versus percent diluent for stoichiometric ethylene-oxygen-nitrogen mixture is shown in Figure 25 for each obstacle configuration. All DDT time data appears in Appendix D. The DDT time data follows the same trends as the DDT distance data. Experiments were performed over a range of 0% to 73.8% diluent. As previously mentioned, detonations failed to occur for higher amounts of diluent. DDT time versus initial pressure for stoichiometric ethylene-oxygen-nitrogen mixture is shown in Figure 26 for each obstacle configuration. Experiments were performed over a range of 30 kPa to 100 kPa. Analogous to the DDT distance results, the presence of obstacles decreases the DDT time to the same proportion as it decreases the distance, regardless of whether or not orifice plates or blockage plates are used.



**Figure 25. DDT time for varying diluent and obstacle configurations**

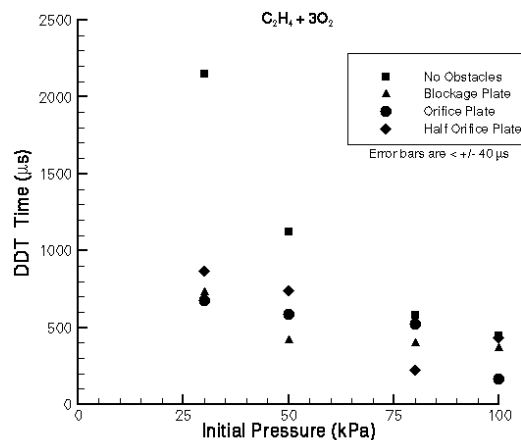


**Figure 26. DDT time versus pressure and obstacle configurations**

## 5.2 Impulse

### 5.2.1 Effect of Diluent Concentration, Pressure and Obstacle Configuration on Impulse

#### 5.2.1.1 Effects of Diluent Concentration

Impulse normalized by tube volume versus diluent concentration for different stoichiometric ethylene-oxygen-nitrogen mixtures can be seen in Figure 27 for each obstacle configuration. All additional impulse data appears in Appendix E. Experiments were performed over a range of 0% to 73.8% diluent. A line of predicted impulse that is expected from a tube with immediate detonation and no obstacles is also included. This data comes from the theoretical model previously described. The data show that higher diluent concentrations result in lower impulse for both ballistic and pressure impulses. The DDT limit for diluent concentration was found to be 60% after which DDT would not occur. At this limit, the inclusion of diluent resulted in a 30% impulse loss as compared to the 0% diluent case.

The presence of diluent lessens the amount of fuel present in a given volume of a mixture, and thus lowers the amount of energy that can be released.

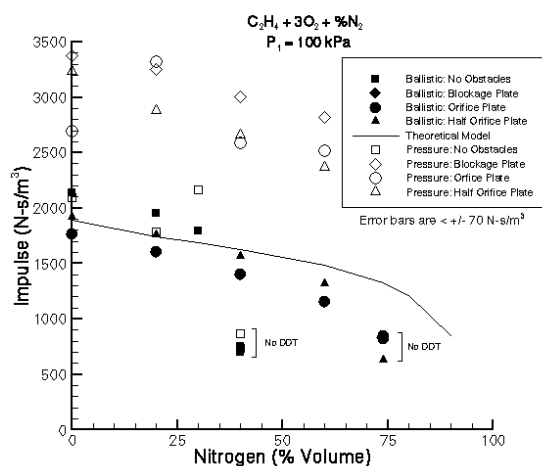


**Figure 27. Impulse for varying diluent and obstacle configurations**

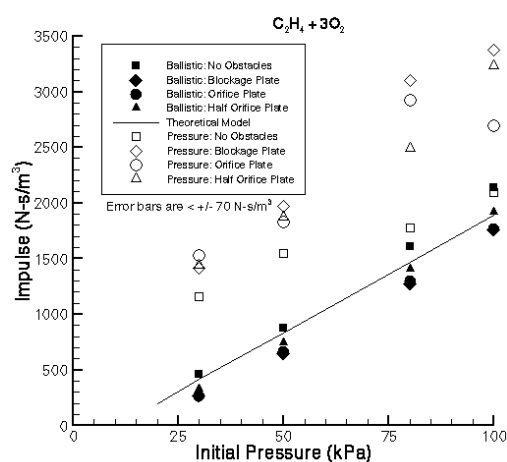


**Figure 28. Impulse versus pressure and obstacle configurations**

### 5.2.1.2 Effects of Mixture Pressure

Impulse normalized by tube volume versus initial mixture pressure can be seen in Figure 28 for each obstacle configuration. Experiments were performed over a range of 30 kPa to 100 kPa initial pressure. A line of predicted impulse that is expected from a tube with immediate detonation and no obstacles is also included. This data comes from the theoretical model previously described. The mixture was found to DDT over the entire range of pressures tested. Decreasing the initial pressure was observed to decrease the impulse in what appears to be a linear fashion for both ballistic and pressure impulses. At 30 kPa, the lowest test pressure, impulse losses of 75% were observed as compared to 100 kPa cases.

Initial pressure corresponds to increased density, allowing for more fuel to be present in a given volume. This allows for higher energy release per unit volume. Higher pressure also increases the likelihood of the combustion reaction to occur. Increased pressure causes the chemical kinetics to increase, higher reaction rate...

### 5.2.1.3 Effect of Obstacles

The addition of obstacles was found to produce different results for the ballistic and pressure impulses. In the ballistic impulse calculation, obstacle inclusion resulted in the lowering of impulse by about 25%. In the pressure impulse calculation, obstacle inclusion resulted in varying increases in impulse. This is attributed the inability of the pressure impulse model to account for obstacle drag and is discussed below.

### 5.2.2 Comparison of Ballistic and Pressure Impulse Methods

All impulses obtained from pressure measurements are higher than the ballistic pendulum measurements by an average value of about 100% for the cases with internal obstacles.

This is attributed to the pressure and viscous drag losses over the obstacles. Note that the no obstacle configuration ballistic and pressure impulses match the closest, as would be expected if the obstacle drag was eliminated (by the elimination of obstacles). For experiments with no obstacles, there was no obstacle drag and thus, the pressure impulse was within 15% of the ballistic impulse for cases where DDT occurred while varying diluent and pressure, except at low pressures where the percent difference increased to approximately 40%. The half orifice plates match the second best since they have only half the surface area of the full orifice and blockage plates.

By determining the average percent difference between the impulse calculated from the pressure integration and ballistic pendulum methods for each obstacle configuration, several conclusions may be drawn. These results appear below in figure 29 and are averaged across all runs with varying pressure and diluent concentration. The no obstacle case has an average percent different of approximately 20%. This percent loss in impulse of the ballistic measurement as compared to the pressure integration may be attributed to losses at the interior tube walls that the pressure integration does not account for. The losses in the blockage plates were the greatest with a 60% loss in impulse. The full orifice plates contained the next highest loss in impulse with a 55% loss in impulse. The half orifice plates obstacle configuration generated the least amount of impulse loss as would be expected since there is less obstruction of the flow. These results show that although internal obstacles can enhance DDT they can significantly impact the resulting impulse and should be minimized while still providing the desired transition to detonation.

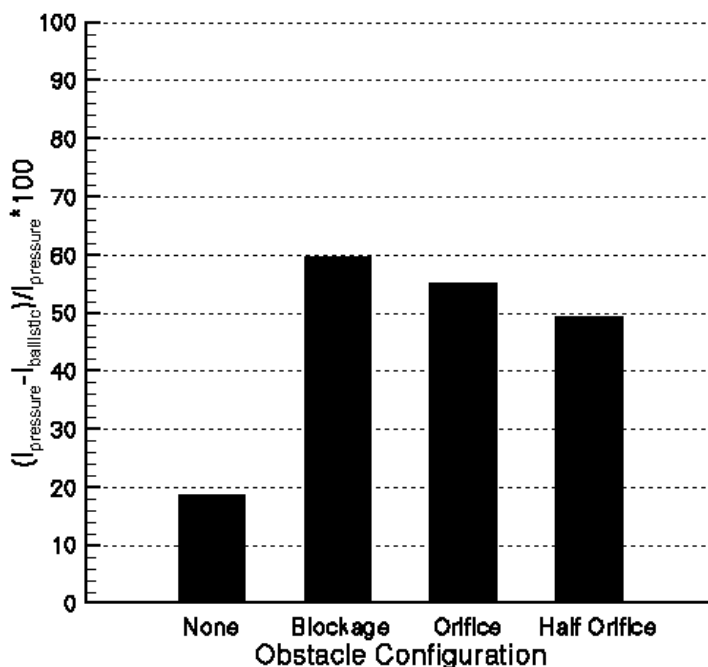


Figure 29. Comparison of drag due to internal obstacles

### 5.2.3 Theoretical Impulse Model

Ballistic impulse data for no obstacles correlates well with the expected impulse model for a no obstacle tube for varying both the diluent and the pressure. For obstacle cases, increased drag lowers the resulting ballistic impulse from theory by about 25%. For the same cases, the pressure impulse exhibits at least a 100% increase in impulse as compared to the no obstacle case. This can be attributed to the neglecting of the pressure drag on the obstacles as discussed previously. Out of all the obstacle cases, the half orifice plate configuration is the closest to theory. This confirms that obstacle drag is the most significant contributor to the difference between the model and the data.

## 6.0 Discussion and Conclusions

DDT time and distance have been reported. These results were obtained for a set of stoichiometric ethylene-oxygen-nitrogen mixtures varying the diluent, pressure, and obstacle configuration of the mixture. Experimental impulse measurements were determined by two independent methods and have also been reported.

### 6.1 DDT Distances and DDT Times

DDT distances and DDT times were found to decrease with the introduction of obstacles into the flow. The decrease becomes more apparent at lower pressures and higher amounts of diluent. Given the experimental error, it is not possible to determine whether there is a significant difference in the DDT distance and time between the blockage plate configuration and the orifice plate configuration. Further experiments would have to be performed with the ion probes at more frequent intervals allowing the DDT position and time to be obtained at a higher resolution. In addition, the repeatability of DDT time and position should be explored.

### 6.2 Impulse

#### 6.2.1 Effect of Diluent Concentration, Pressure and Obstacle Configuration on Impulse

The impulse was found to increase with increasing pressure and decreasing diluent. The presence of obstacles in the flow results in a dramatically lower impulse than if DDT were to occur in a clean tube. This loss is attributed to the pressure and viscous drag from flow over the obstacle configuration. However, the obstacles enable DDT to occur at mixtures where it would normally not in a clean tube, and thus produce more impulse than a clean tube under these conditions.

#### 6.2.2 Comparison of Ballistic and Pressure Impulse Methods

The method of determining impulses by integrating the pressure traces on the front wall does not take into account flow losses such as drag and friction on the tube and obstacle surfaces. For experiments with no obstacles, there was no obstacle drag and thus, the pressure impulse was close to the ballistic impulse for cases where DDT occurred while varying diluent and pressure, except at low pressures where the percent difference increased to approximately 40%. The pressure impulse model's lack of a mechanism to model the obstacle drag resulted in higher pressure impulses than were obtained from the ballistic impulse, which accounts for all losses.

#### 6.2.3 Theoretical Impulse Model

Ballistic impulse data for no obstacles correlates well with the expected impulse model for a no obstacle tube for varying both the diluent and the pressure. For obstacle cases, increased drag lowers the resulting impulse from theory by about 25%. In future work,

the theoretical model should be updated to account for increased drag due to obstacle inclusion. To maximize the impulse obtained, obstacles should only be included in the tube until the DDT distance, since the obstacles are designed only to create turbulence to promote DDT. Such a setup will expedite the onset of DDT while minimizing losses incurred from the detonation wave passing over the obstacles. The half orifice plate obstacle was used to approximate this design and did reduce the losses somewhat, while still effectively inducing DDT.

#### 6.2.4 Additional Loss Mechanisms

Another process that contributes to impulse loss in this experimental setup is the occurrence of late DDT. If a deflagration wave propagates long enough down the length of the tube, it compresses the unburned gas ahead of it enough to rupture the diaphragm. This results in much of the ethylene-oxygen-nitrogen mixture being pushed into the atmosphere, where its combustion will not contribute significantly to the impulse. The onset of a detonation wave can mitigate this effect somewhat due to the higher propagation speed associated with a detonation wave. It is possible for a detonation wave to overtake the compression waves from the previous detonation before enough compression waves reach the diaphragm to rupture it as shown in Figure 30. This loss is expected to become pronounced when DDT occurs in the last quarter of the tube, and the detonation wave does not have enough time to catch up to the deflagration compression waves.

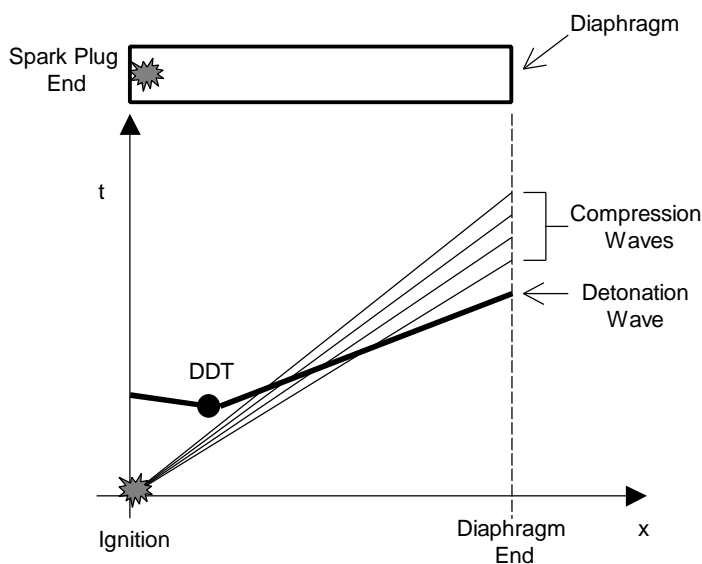


Figure 30. Late DDT

### 6.3 Future Work

This study is part of a large program examining DDT and detonation phenomena and how they apply to pulse detonation engines. In future work higher resolution DDT time and distance data should be obtained, with attention paid to reproducibility. A theoretical

model needs to be created to take into account obstacle drag. Also, more extensive testing of different obstacle geometries and blockage ratios is needed as well as the investigation of the effect of varying the fuel and equivalence ratio of the combustible mixture. Particularly desirable is the design of obstacle configurations that will allow DDT to occur early in mixtures with diluent concentrations similar to air.

## **Acknowledgement**

This study was carried out as partial fulfillment of graduate education requirements for the class Ae104c at Caltech. Funding for the research has been provided in part by the GE – PO A0281655 under DABT-63-0-0001, MURI PDE (grant 00014-99-1-0744, subcontract 1686-ONR-0744), Graduate Aeronautical Laboratories and the Mechanical Engineering Department at the California Institute of Technology, and by the National Defense Science and Engineering Graduate Fellowship Program. Thanks to Joanna Austin and Eric Wintenberger for their support and very special thanks to Dr. Eric Schultz whose guidance was crucial to the completion of this study.

# Appendix A

Shot #	Date	Series											Impulse Measurements (kg.m/s)				
			P1 (kPa)	T1 (K)	Moles Fuel	Fuel	Moles Ox	Ox	% Dil	Moles Dil	Dil	Vcj (m/s)	Pcj (MPa)	dx (mm)	Bob Mass (kg)	Swing impulse	Normalized Swing Impulse
37	5/3/00	104c: No Obstacles	50	297	1	C2H4	3	O2	0	0.00	N2	2342.6	1.654	121	13.274	4.037	881.643
38	5/4/00	104c: No Obstacles	50	297	1	C2H4	3	O2	0	0.00	N2	2342.6	1.654	121	13.274	4.037	881.643
39	5/4/00	104c: No Obstacles	30	297	1	C2H4	3	O2	0	0.00	N2	2318.0	0.973	64	13.274	2.134	466.069
40	5/4/00	104c: No Obstacles	80	297	1	C2H4	3	O2	0	0.00	N2	2365.4	2.693	220	13.274	7.353	1605.815
41	5/4/00	104c: No Obstacles	100	297	1	C2H4	3	O2	0	0.00	N2	2376.0	3.394	292	13.274	9.779	2135.507
42	5/4/00	104c: No Obstacles	100	297	1	C2H4	3	O2	20	1.00	N2	2258.8	3.017	267	13.274	8.935	1951.227
43	5/5/00	104c: No Obstacles	100	297	1	C2H4	3	O2	40	2.67	N2	2132.3	2.640	96	13.274	3.202	699.289
44	5/5/00	104c: No Obstacles	100	297	1	C2H4	3	O2	30	1.71	N2	2198.0	2.830	246	13.274	8.228	1796.738
45	5/5/00	104c: BR = 0.43 Blockage Plates with 3" Spacing	100	297	1	C2H4	3	O2	40	2.67	N2	2132.3	2.640	175	13.975	6.152	1402.194
46	5/5/00	104c: BR = 0.43 Blockage Plates with 3" Spacing	100	297	1	C2H4	3	O2	60	6.00	N2	1977.1	2.230	144	13.975	5.060	1153.211
47	5/6/00	104c: BR = 0.43 Blockage Plates with 3" Spacing	100	297	1	C2H4	3	O2	73.8	11.27	N2	1824.8	1.862	104	13.975	3.653	832.446
48	5/6/00	104c: BR = 0.43 Blockage Plates with 3" Spacing	100	297	1	C2H4	3	O2	20	1.00	N2	2258.8	3.017	200	13.975	7.035	1603.293
49	5/6/00	104c: BR = 0.43 Blockage Plates with 3" Spacing	100	297	1	C2H4	3	O2	0	0.00	N2	2376.3	3.390	220	13.975	7.742	1764.399
50	5/6/00	104c: BR = 0.43 Blockage Plates with 3" Spacing	30	297	1	C2H4	3	O2	0	0.00	N2	2318.0	0.973	33	13.975	1.158	264.008
51	5/6/00	104c: BR = 0.43 Blockage Plates with 3" Spacing	50	297	1	C2H4	3	O2	0	0.00	N2	2342.6	1.650	81	13.975	2.844	648.204
52	5/6/00	104c: BR = 0.43 Blockage Plates with 3" Spacing	80	297	1	C2H4	3	O2	0	0.00	N2	2365.4	2.690	159	13.975	5.588	1273.639
53	5/6/00	104c: No Obstacles	50	297	1	C2H4	3	O2	0	0.00	N2	2342.0	1.650	121	13.274	4.037	881.643
54	5/6/00	104c: No Obstacles	100	297	1	C2H4	3	O2	40	2.67	N2	2132.6	2.640	104	13.274	3.469	757.626
55	5/9/00	104c: BR = 0.43 14-Orifice Plates with 3" Spacing	100	297	1	C2H4	3	O2	73.8	11.27	N2	1824.8	1.862	102	14.28394	3.661	853.677
56	5/9/00	104c: BR = 0.43 14-Orifice Plates with 3" Spacing	100	297	1	C2H4	3	O2	60	6.00	N2	1977.1	2.230	138	14.28394	4.956	1155.493
57	5/9/00	104c: BR = 0.43 14-Orifice Plates with 3" Spacing	100	297	1	C2H4	3	O2	40	2.67	N2	2132.2	2.640	168	14.28394	6.036	1407.360
58	5/9/00	104c: BR = 0.43 14-Orifice Plates with 3" Spacing	100	297	1	C2H4	3	O2	20	1.00	N2	2258.8	3.017	192	14.28394	6.902	1609.138
59	5/9/00	104c: BR = 0.43 14-Orifice Plates with 3" Spacing	30	297	1	C2H4	3	O2	0	0.00	N2	2318.0	0.973	32	14.28394	1.148	267.690
60	5/9/00	104c: BR = 0.43 14-Orifice Plates with 3" Spacing	50	297	1	C2H4	3	O2	0	0.00	N2	2342.6	1.650	80	14.28394	2.871	669.412
61	5/9/00	104c: BR = 0.43 14-Orifice Plates with 3" Spacing	80	297	1	C2H4	3	O2	0	0.00	N2	2365.4	2.690	155	14.28394	5.568	1298.173
62	5/9/00	104c: BR = 0.43 14-Orifice Plates with 3" Spacing	100	297	1	C2H4	3	O2	0	0.00	N2	2375.3	3.390	211	14.28394	7.588	1769.084
63	5/9/00	104c: BR = 0.43 14-Orifice Plates with 3" Spacing	100	297	1	C2H4	3	O2	73.8	11.27	N2	1824.8	1.862	99	14.28394	3.554	828.543
64	5/18/00	104c: BR = 0.43 7-Orifice Plates with 3" Spacing	100	297	1	C2H4	3	O2	73.8	11.27	N2	1824.8	1.862	78	14.02089	2.748	630.318
65	5/18/00	104c: BR = 0.43 7-Orifice Plates with 3" Spacing	100	297	1	C2H4	3	O2	60	6.00	N2	1977.1	2.230	163	14.02089	5.748	1318.605
66	5/18/00	104c: BR = 0.43 7-Orifice Plates with 3" Spacing	100	297	1	C2H4	3	O2	40	2.67	N2	2132.2	2.640	193	14.02089	6.810	1562.164
67	5/18/00	104c: BR = 0.43 7-Orifice Plates with 3" Spacing	100	297	1	C2H4	3	O2	20	1.00	N2	2258.8	3.017	217	14.02089	7.661	1757.328
68	5/18/00	104c: BR = 0.43 7-Orifice Plates with 3" Spacing	30	297	1	C2H4	3	O2	0	0.00	N2	2318.0	0.973	41	14.02089	1.444	331.245
69	5/18/00	104c: BR = 0.43 7-Orifice Plates with 3" Spacing	50	297	1	C2H4	3	O2	0	0.00	N2	2342.6	1.650	92	14.02089	3.241	743.543
70	5/18/00	104c: BR = 0.43 7-Orifice Plates with 3" Spacing	80	297	1	C2H4	3	O2	0	0.00	N2	2365.4	2.690	174	14.02089	6.137	1407.863
71	5/18/00	104c: BR = 0.43 7-Orifice Plates with 3" Spacing	100	297	1	C2H4	3	O2	0	0.00	N2	2375.3	3.390	237	14.02089	8.371	1920.210

## Ballistic Pendulum Experiment Checklist

Shot #		Operators:	
Date:		Time:	
Obstacle configuration:			
Total Mass:			

### Preparation and Pump Down

1.  Ensure spark plug is disconnected and shorted
2.  Insert diaphragm and label shot number
3. Connect:  Pressure transducers ( Blast gauge)  
 Spark box to DG535  Camera controller to video  
 TV and video
4. Check:  Camera is focussed  Camera is mounted in casing  
 Fiducial is aligned  All optics are bolted down  
 Camera view is unobstructed  PCB cables are free to move
5. Turn on:  DG535  Oscilloscope  
 PCB power supplies  Video  
 Camera controller  TV  
 Halogen lamp
6.  Seal PCB power supply and camera controller casing
7.  Close fuel, oxidizer, diluent bottle valves
8.  Close vacuum pump vent valve
9. Open:  Vacuum pump isolation valve  Fuel, oxidizer, diluent fill valves  
 Tube valves  Test section isolation valve  
 Pressure gauge valves  Vacuum pump vent valve
10. On:  Vacuum pump  Vacuum gauge
11.  Close vacuum pump vent valve
12.  Wait for pressure to drop below 800 mTorr
13. Off:  Fill needle valve
14. Open:  Bottle valves
15. On:  Regulator valves
16. Off:  Fill gauge valve
17.  Wait for pressure to drop below 100 mTorr

### Gas Fill Procedure

18.  Prepare gas fraction/pressure table below:
19.  Check doors are closed
20.  Turn on warning lights. Lab access restricted.

(time sensitive part)

21. \_\_\_ Close vacuum pump isolation valve
22. Off: \_\_\_ Vacuum gauge
23. \_\_\_ Open vacuum vent valve
24. Off: \_\_\_ Vacuum pump
25. \_\_\_ Zero pressure gauge
26. \_\_\_ Fill each gas to desired pressure (record final pressures)

Gas	Target Fraction	Target Partial Pressure	Target Final Pressure	Final Pressure
		mbar	mbar	mbar
		mbar	mbar	mbar
		mbar	mbar	mbar
		mbar	mbar	mbar

27. Close: \_\_\_ Fuel, oxidizer, diluent fill valves  
 \_\_\_ Fuel, oxidizer, diluent regulator valves  
 \_\_\_ Fuel, oxidizer, diluent bottle valves  
 \_\_\_ Test section isolation valve
28. \_\_\_ Run circulation pump for 5 minutes Pump on at: \_\_\_\_\_
29. \_\_\_ Shut off pump
30. \_\_\_ Wear ear and eye protection
31. \_\_\_ Close tube valves in test room (Combustible mixture in tube and fill lines.)
32. On: \_\_\_ Vacuum pump
33. \_\_\_ Close vacuum pump vent valve
34. Open: \_\_\_ Vacuum pump isolation valves \_\_\_ Fuel, oxidizer, diluent fill valves  
 \_\_\_ Test section isolation valve individually  
 \_\_\_ Vacuum gauge
35. Close: \_\_\_ Fuel, oxidizer, diluent fill valves  
 \_\_\_ Test section isolation valve  
 \_\_\_ Pressure gauge valves \_\_\_ Vacuum pump isolation valve
36. \_\_\_ Wear ear and eye protection
37. \_\_\_ Disconnect tube fill lines (Combustible mixture only in tube.)
38. \_\_\_ Cap off tube fill lines
39. \_\_\_ Close experiment room door
40. Turn: \_\_\_ A1 to vent \_\_\_ A2 to air

### Firing Procedure

41. \_\_\_ Arm oscilloscope
42. \_\_\_ Record video
43. \_\_\_ Connect spark cable to spark box
44. \_\_\_ Turn on spark box
45. \_\_\_ Warn lab occupants
46. \_\_\_ **CHECK all valves are closed**
47. \_\_\_ Trigger DG535 to fire
48. \_\_\_ Stop video
49. Turn: \_\_\_ A2 to vent \_\_\_ A1 to air
50. \_\_\_ Turn off spark box
51. \_\_\_ Disconnect spark cable and short

52. \_\_\_ Turn off warning lights  
 53. \_\_\_ Save and process data  
 54. \_\_\_ Wait 5 minutes to vent room (crack door open after 1 minute).
55. Turn off: \_\_\_ Camera controller \_\_\_ DG535  
 \_\_\_ PCB power supplies \_\_\_ Oscilloscope  
 \_\_\_ TV \_\_\_ Video  
 \_\_\_ Halogen lamp \_\_\_ Vacuum pump

**Data:**

56. Data Saved on Disk \_\_\_\_\_

<b>Filenames:</b>		<b>PCB:</b> $\Delta x = 0.5207, 0.41656$ m		<b>Ionization Probes:</b> $\Delta x = 0.10414$ m		
Ion data:		#	Time	#	Time	Velocity
PCB 1:		1 @0.0381 m	$\mu$ s	1 @0.0381 m	$\mu$ s	m/s
PCB 3:		3 @0.5588 m	$\mu$ s	2	$\mu$ s	m/s
PCB 4:		4 @0.97536 m	$\mu$ s	3	$\mu$ s	m/s
				4	$\mu$ s	m/s
<b>Scope:</b>		<b>Deflection:</b>		5	$\mu$ s	m/s
Sample rate:		Initial:	mm	6	$\mu$ s	m/s
PCB scale:		Max:	mm	7	$\mu$ s	m/s
Ion scale:		$\Delta x$	mm	8	$\mu$ s	m/s
		Impulse:	N-s	9	$\mu$ s	m/s
<b>Theory:</b>				10	$\mu$ s	m/s
$V_{ci}$ :	m/s					
$P_{ci}$	bar					

57. \_\_\_ Check PCB traces for thermalization.

**Comments:**

## **Appendix B**

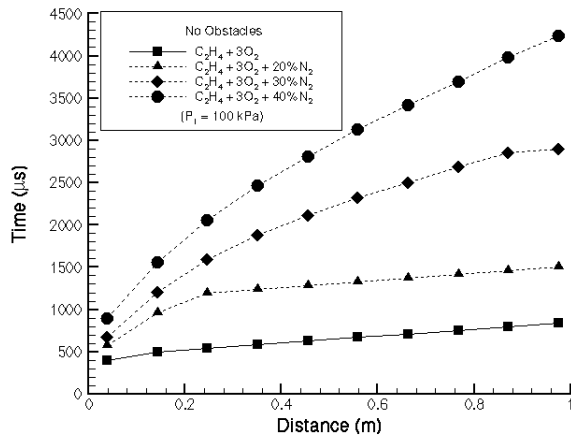


Figure B-1: Varying diluent with no obstacles

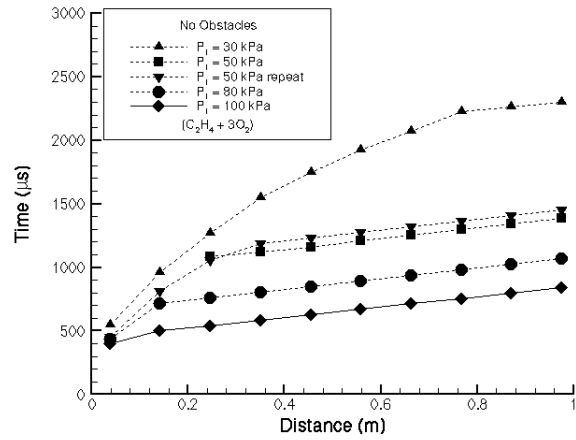


Figure B-2: Varying pressure with no obstacles

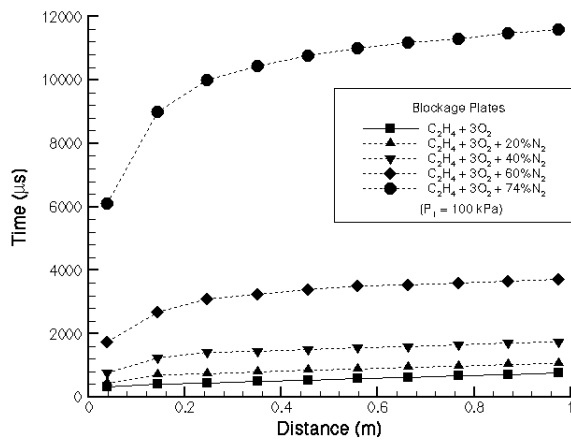


Figure B-3: Varying diluent with blockage plates

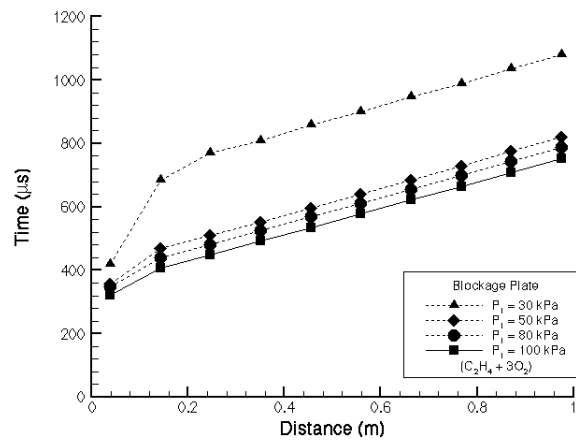


Figure B-4: Varying pressure with blockage plates

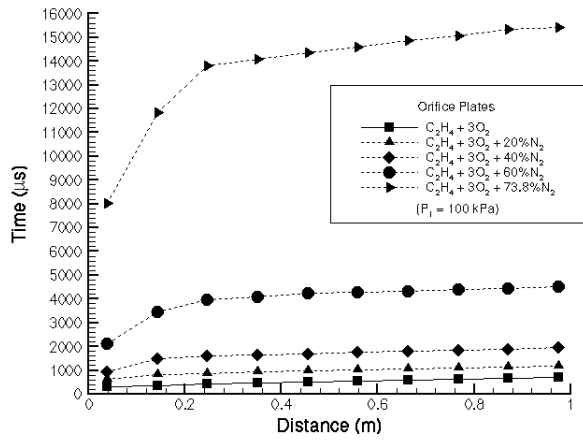


Figure B-5: Varying diluent with orifice plates

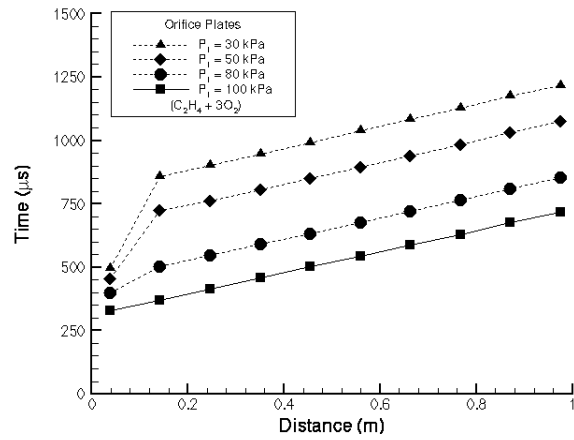


Figure B-6: Varying pressure with orifice plates

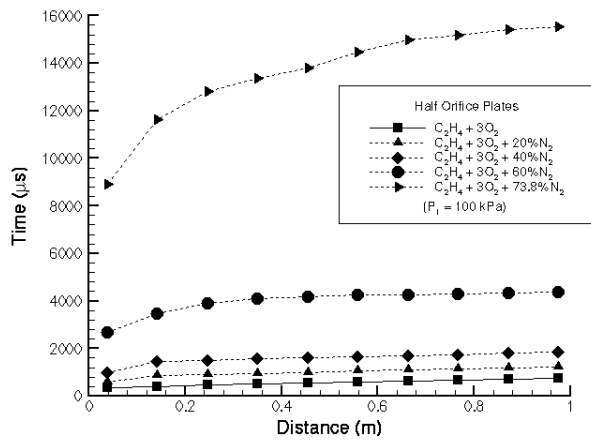


Figure B-7: Varying diluent with half orifice plates

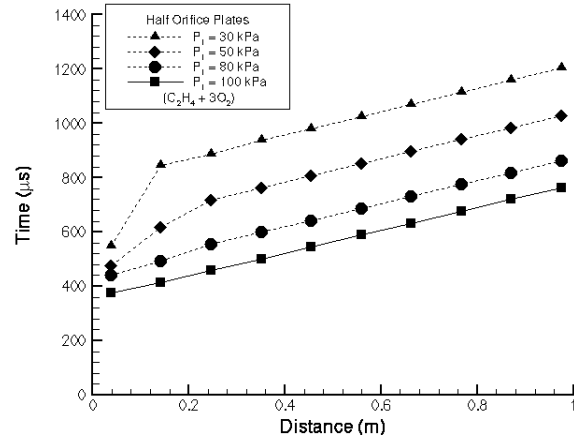


Figure B-8: Varying pressure with half orifice plates

## **Appendix C**

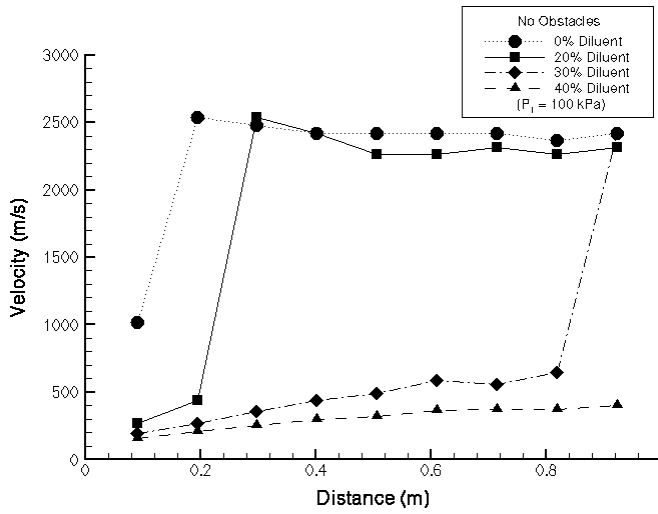


Figure C-1: Varying diluent with no obstacles

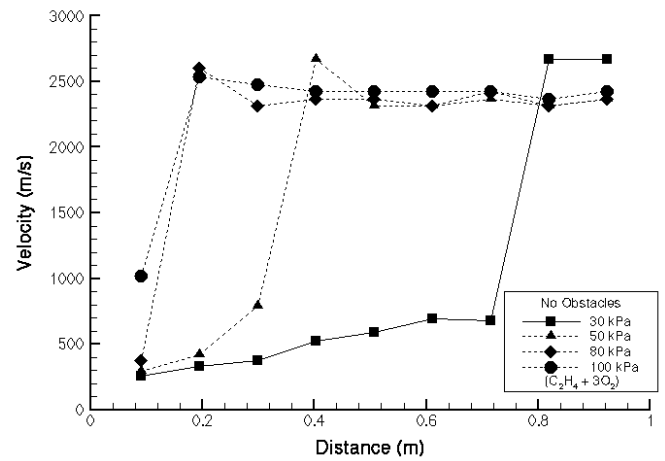


Figure C-2: Varying pressure with no obstacles

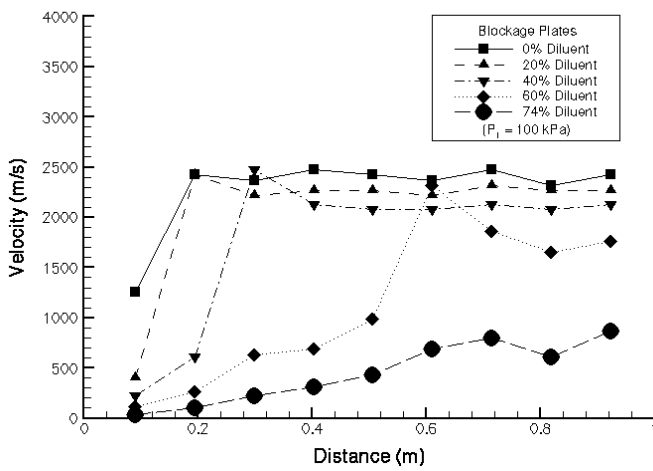


Figure C-3: Varying diluent with blockage plates

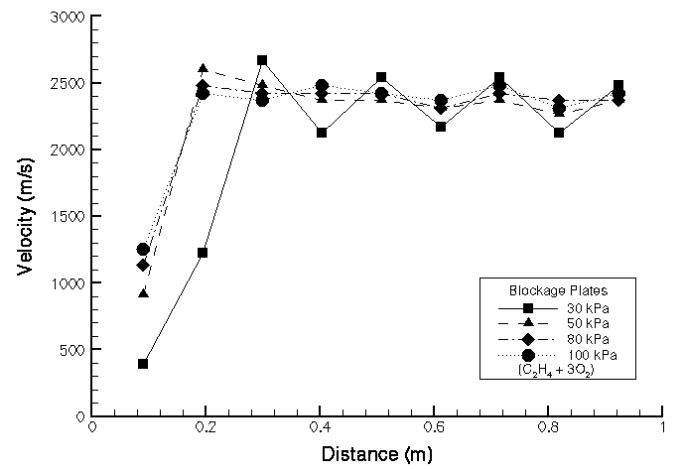


Figure C-4: Varying pressure with blockage plates

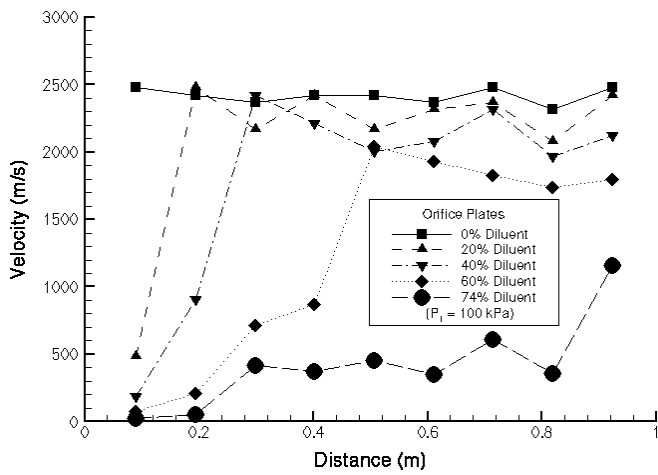


Figure C-5: Varying diluent with orifice plates

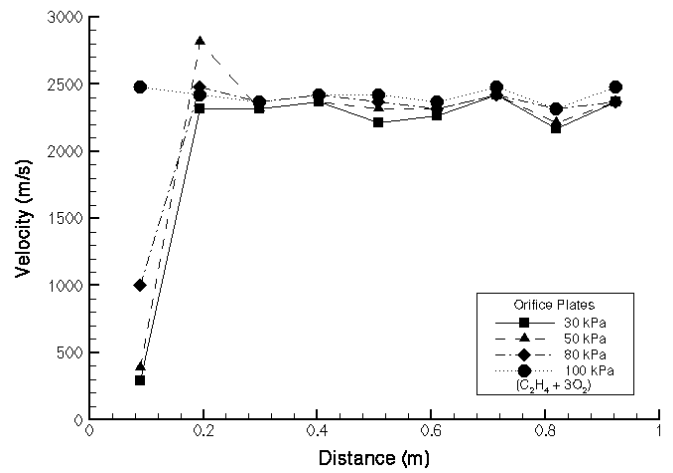


Figure C-6: Varying pressure with orifice plates

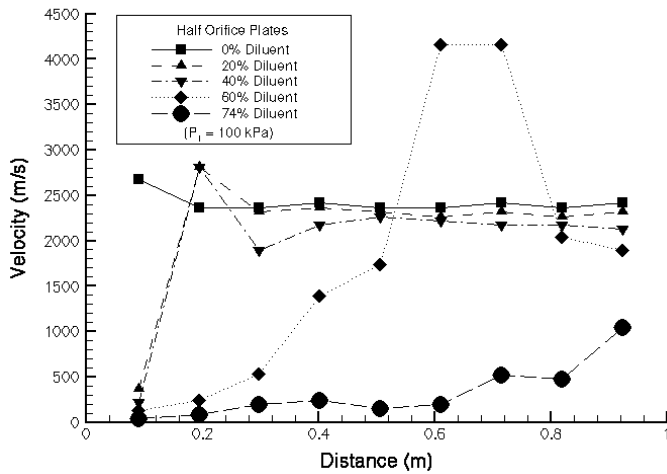


Figure C-7: Varying diluent with half orifice plates

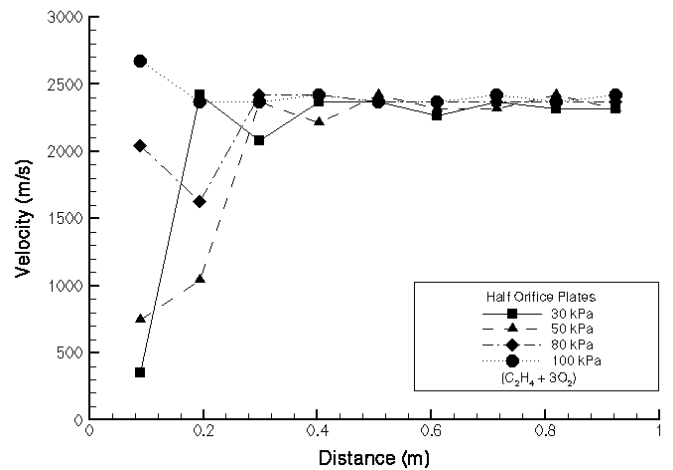


Figure C-8: Varying pressure with half orifice plates

## **Appendix D**

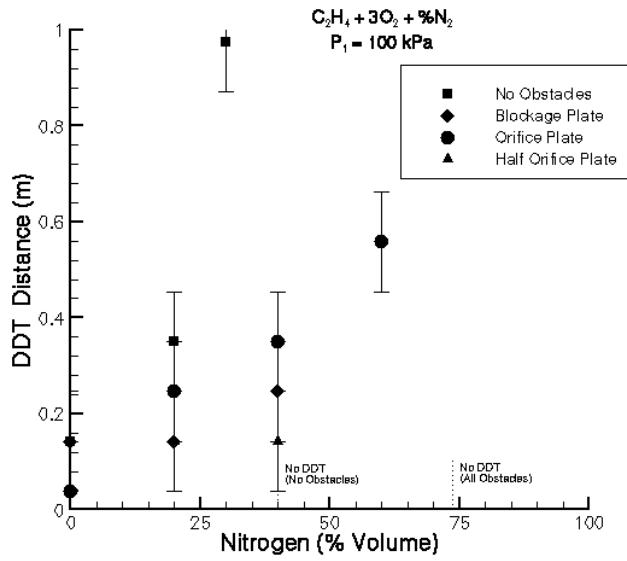


Figure D-1: Varying diluent

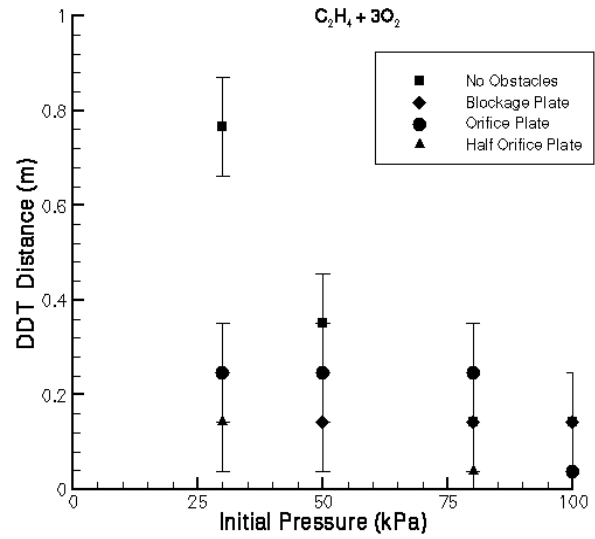


Figure D-2: Varying pressure

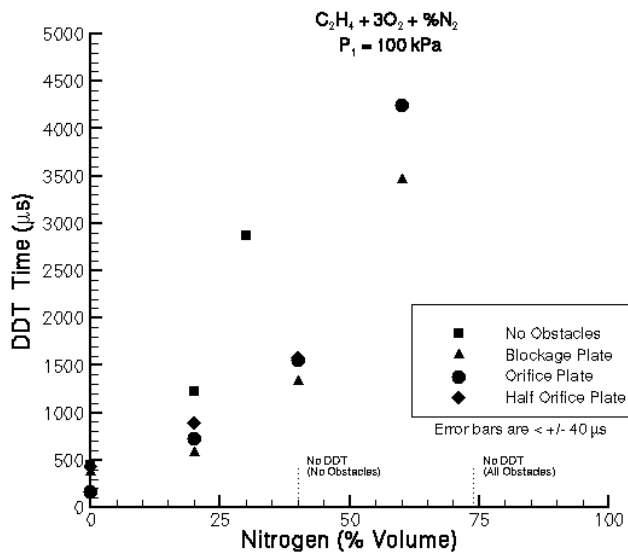


Figure D-3: Varying diluent

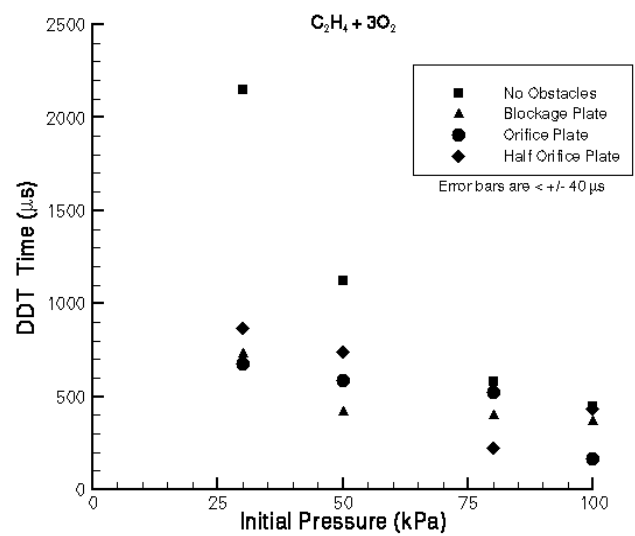


Figure D-4: Varying pressure

## **Appendix E**

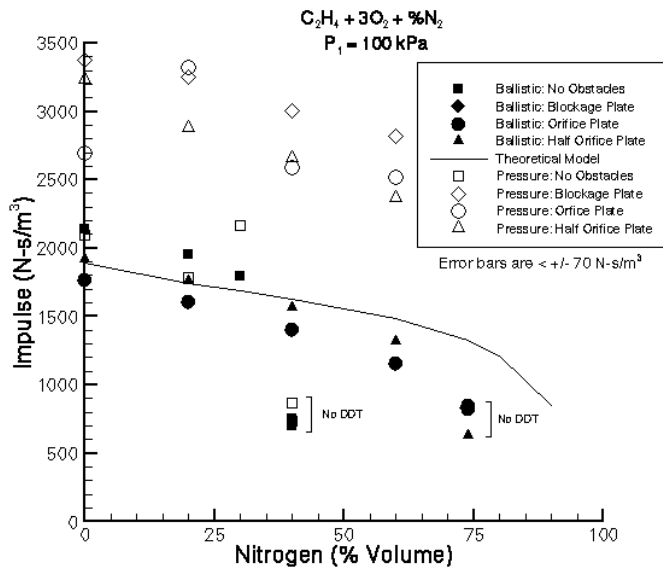


Figure E-1: Varying diluent

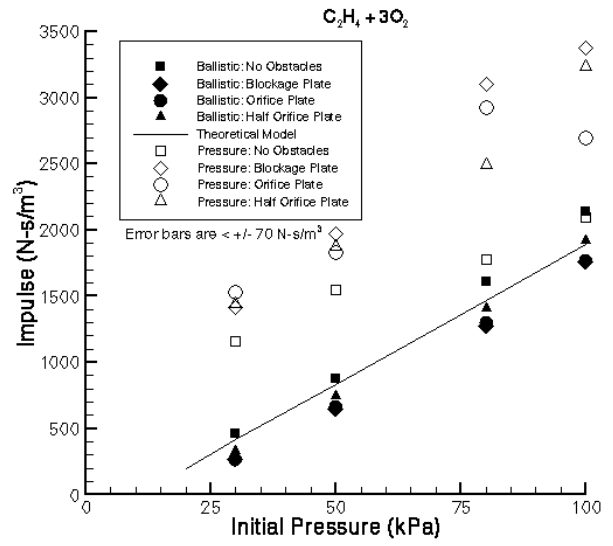


Figure E-2: Varying pressure